Journal of Zhejiang University-SCIENCE A in press
www.jzus.zju.edu.cn; www.springer.com/journal/11582
E-mail: jzus_a@zju.edu.cn

Research Article
https://doi.org/10.1631/jzus.A2500490

Flow structure and mixing characteristics of a transverse jet in supersonic crossflow under varied boundary layers

Yanhui ZHAO[1], Zhenfeng WANG[2], Shunping ZHANG[1], Shimao WANG[2], Xuechen LI[2], Ye TIAN[2]✉

[1]*National Key Laboratory of Ramjet, Mianyang 621000, China*
[2]*Key Laboratory of Cross-Domain Flight Interdisciplinary Technology, Mianyang 621000, China*

Abstract: Efficient fuel – air mixing within milliseconds is critical for scramjet performance, yet the flow physics of a transverse jet in supersonic crossflow remains insufficiently quantified. Planar Rayleigh/Mie scattering and stereoscopic particle-image velocimetry were applied to a Mach 2.68 crossflow. Jets with a 2 mm orifice diameter were injected at three dynamic-pressure ratios (1.64, 4.92, and 8.19) under two incoming boundary layer thicknesses (1 mm and 4 mm). Instantaneous imaging captured the bow shock, barrel shock, Mach disk, slip line, recirculation zone, and counterrotating vortex pair. Vorticity fields revealed streamwise vortices forming beside the barrel shock, merging 20 mm downstream from the jet orifice, and persisting as a typical counterrotating vortex pair that entrained freestream fluid. Boundary layer thickness systematically enhanced jet penetration and modulates near-field breakup patterns without altering far-field mixing limits. The penetration depth was fitted using a modified correlation, indicating an approximately 10-20% increase when the boundary layer thickness increased from 1 mm to 4 mm. Lateral diffusion reached 15 mm at the orifice and plateaued at 20 mm beyond 20 mm downstream from the jet orifice. Fractal analysis partitioned the jet plume edges into three regions. A thicker boundary layer elevated the initial fractal dimension in Region I but suppressed its growth in Region II, whereas Region III exhibited consistent rapid fragmentation. The quantitative datasets and key parameters established benchmarks for validating computational fluid dynamics simulations and scramjet engine designs.

Key words: Jet in supersonic crossflow; Streamwise vortices; Penetration depth and lateral diffusion; Fractal dimension; Breakup process

1 Introduction

In scramjet engines, the mainstream flow remains supersonic throughout the combustion chamber. Consequently, the residence time of injected fuel is limited to milliseconds, imposing significant challenges for achieving complete fuel–air mixing (Huang et al., 2019), ignition (Sun et al., 2020), flame propagation and stable combustion (Shi et al., 2020) within this constrained duration. These limitations constitute a critical bottleneck for attaining high engine performance (Huang, 2016). In engine design, it is essential to enhance mixture formation for combustion mode transition while minimizing total pressure loss (Liao et al., 2018) and to maximize combustion stability and combustion efficiency to the greatest extent possible (Jia et al., 2022). Transverse fuel injection represents the most prevalent and effective fueling strategy for supersonic inflows (Huang et al., 2020). Steinberg et al. (Steinberg et al., 2013) experimentally investigated the combustion characteristics of transverse hydrogen jets, revealing that flames stabilize in two distinct branches along the jet centerline: one anchored in the jet leeward region and another lifted above the jet trajectory. The leeward-stabilized branch exhibits superior positional stability under high jet velocities due to large-scale recirculation zones downstream of the orifice, whereas the lifted branch demonstrates greater dynamic variability. Similar flame stabilization regimes reported by Gamba Mirko et al. (Gamba and Mungal, 2015) and Zhang et al. (Zhang et al., 2021a) further corroborate the efficacy of transverse injection configurations.

Mixing constitutes the initial physical process governing downstream combustion performance.

✉ Ye TIAN, tianye@cardc.cn
Ye TIAN, https://orcid.org/0000-0001-9955-3438

Received Oct. 13, 2025; Revision accepted Mar. 27, 2026;
Crosschecked

Accordingly, characterizing the flow field structure and mixing dynamics of transverse jets in supersonic crossflow is critical for optimizing scramjet combustors. Liu et al. (Liu et al., 2015; Liu et al., 2019) demonstrated that recirculation zones and vortical structures facilitate ignition, flame propagation, and stabilization, whereas intensified fuel–air mixing and enlarged reaction interfaces augment combustion efficiency. Zhang et al. (Zhang et al., 2023) conducted a parametric investigation of a transverse jet injected into a model combustor at Mach 1.2 and 2.5. Their measurements revealed that although the lower Mach configuration exhibits diminished separation bubbles and reduced large-scale coherent motions—hence weaker vortical transport—the prolonged fuel residence time compensates by enhancing turbulent and molecular diffusion, leading to superior mixing effectiveness and combustion efficiency at the lower Mach number.

Research on supersonic transverse jets has evolved from fundamental flat-plate studies. Pioneering work by Glagolev et al. (Glagolev et al., 1967) established the core gas dynamic scheme—a lambda-shaped shock system and three-dimensional separated flow with horseshoe vortices—via schlieren and oil-flow visualization. Their subsequent research (Glagolev et al., 1971) quantified jet geometry using an "equivalent solid obstacle" analogy, correlating spread and penetration with the dynamic pressure ratio through models based on momentum balance and blast-wave theory, leading to empirical formulas. The effect of surface geometry was explored by Zubkov et al. (Zubkov et al., 1994) for a jet issuing from the edge of a 90° dihedral angle, revealing a thicker boundary layer, longer separation zone, and internal flow convergence lines indicative of more complex vortex structures than those on a flat surface. For a jet on a conical body, Anokhin et al. (Anokhin et al., 1998) developed a method using multiangle schlieren photographs of a rotated model to reconstruct the full three-dimensional shape of the bow shock. Investigations progressed to annular systems of transverse jets, with Vinogradov et al. (Vinogradov et al., 1999) studying multiple jets arranged circumferentially on a cylinder and identifying flow regimes ranging from independent jet–mainstream interactions to a merged single separation zone ahead of the jets.

Mahesh et al. (Mahesh, 2013) and Zhang et al. (Zhang et al., 2025) summarized the canonical flow features in the flow field of a jet in supersonic crossflow, including vortex structures, jet trajectory, mixing processes, and injectant concentration distribution. Subsequently, the flow field topology of a single transverse jet under supersonic conditions was characterized through experimental and numerical investigations (Vanlerberghe et al., 2013; Liu et al., 2018). Transverse jet injection obstructs the freestream, thereby generating a shock wave system and separation regions near the orifice (Huang and Yan, 2013; Zhang et al., 2021b). Furthermore, high-resolution simulations by Sun et al. (Sun and Hu, 2018a; Sun and Hu, 2018b) and Iwasa et al. (Iwasa and Tsuboi, 2022) resolved detailed vortical structures and the formation mechanism of streamwise vortices.

Santiago et al. (Santiago and Dutton, 1997) acquired detailed velocity distributions of the transverse jet flow structure—including the bow shock, recirculation zone, and counterrotating vortex pair (CVP)—via laser Doppler velocimetry (LDV), demonstrating that counterrotating kidney vortices serve as a primary mixing mechanism with decay rates diminishing gradually downstream. Using temporally resolved Rayleigh/Mie scattering, Gruber et al. (Gruber et al., 1997) revealed that mainstream compressibility modulates large-scale eddy characteristics on the jet windward side. Erdem et al. (Erdem and Kontis, 2021) employed schlieren imaging and particle image velocimetry (PIV) to analyze sonic transverse jets in a Mach 5 crossflow, confirming peak turbulence at the shear layer/shock interaction region. Despite abundant side-view flow visualizations in studies of transverse jets in supersonic crossflow, end-view experimental data remain scarce.

Viti et al. (Viti et al., 2009) demonstrated that boundary layer thickness modulates the formation of streamwise vortices in supersonic crossflow jets. Liu et al. (Liu et al., 2020) established a correlation between turbulent boundary layer characteristics and coherent structures in the transverse jet flow field. Subsequently, Wang et al. (Wang et al., 2013) investigated boundary layer effects on transverse jets using a hybrid RANS/LES approach, revealing that increased boundary layer thickness enhances the

near-field penetration depth and mixing efficiency. Complementarily, Fries et al. (Fries et al., 2021) quantified boundary layer impacts via Mie scattering and schlieren visualization. Their data, compared with prior literature, indicated that turbulent mixing is optimized under distinct conditions: For low molecular weight gases, a thicker boundary layer and lower momentum flux ratios are favorable; for high molecular weight gases, a thinner boundary layer and higher momentum flux ratios yield superior results. The breakup process of the jet plume critically influences mixing and combustion efficiency. A "tilting-stretching-tearing" mechanism was proposed by Ben-Yakar (Ben-Yakar et al., 2006a) to dominate near-field breakup based on schlieren imaging observations. However, quantitative evaluation of this mechanism remains unaddressed.

This study aims to quantify the flow field structure and mixing characteristics of transverse jets through detailed experimental observations. Transient grayscale images and velocity distributions were acquired via planar Rayleigh/Mie scattering and stereoscopic particle image velocimetry (stereo-PIV). Key flow structures, including the barrel shock, Mach disk, slip line, windward shear-layer vortices, CVP, and large-scale eddies, were resolved, while the evolution of streamwise vortices was quantitatively analyzed. Jet penetration depth and lateral diffusion boundaries were extracted via edge-detection algorithms applied to instantaneous images. Furthermore, the plume breakup process was assessed using fractal dimension analysis to quantify mixing efficiency.

2 Experimental setups

2.1 Wind tunnel equipment

To characterize the transverse jet flow field with a turbulent boundary layer, a direct-connect supersonic wind tunnel integrated with a reflector cabin was manufactured. The facility comprises six primary components: a contraction section, stabilization chamber, integrated nozzle/test section, reflector cabin, diffuser, and vacuum tank. More details are available in the literature (Zhao et al., 2020). Notably, to mitigate shock waves induced by assembly misalignment, the integrated nozzle/test section was monolithically fabricated via a B-spline surface design. The reflector cabin is positioned between the test section and the diffuser. An adjustable optical reflector was accommodated at the base of this cabin, while the remaining sides were furnished with large observation windows. The incident laser sheet was redirected by the reflector housed within the chamber. Through precise adjustment of the reflector angle, the laser path was aligned to be nearly parallel to the bottom wall. A schematic diagram of the laser path is presented in Fig.1. Particle imaging analysis corroborated that this design effectively mitigated wall reflection artifacts in the acquired image data.

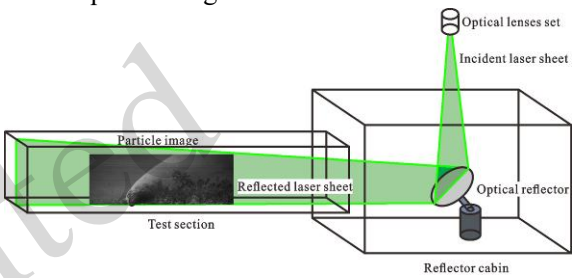

Fig. 1 Observation sketch utilizing a reflector cabin

The test section featured a rectangular cross-section of 120 mm × 56 mm. Optical glass panels mounted on the remaining three walls enabled unobstructed optical observation within a 394 mm (length) × 90 mm (height) field of view that encompassed the concerned region of transverse jet flow field. The total temperature of the mainstream flow in this test section is 300 K, and the total pressure is 1 atm. The Mach number was verified to be 2.68 (Section S1 of the electronic supplementary materials (ESM)). Thus, the static temperature and static pressure can be derived via isentropic relations, as shown in Table 1.

Table 1 Mainstream flow experimental parameters

Experimental parameters	Symbol	Value
Mainstream total temperature	T_0	300 K
Mainstream static temperature	T_∞	123.1 K
Mainstream total pressure	P_0	101325 Pa
Mainstream static pressure	P_∞	4488 Pa
Mainstream velocity	U_∞	596 m/s
Mainstream Mach number	Ma	2.68
Unit Reynolds number	Re_u	9.068×10^6

A jet orifice (2 mm diameter) was integrated at the base of the test section and connected directly to

an upstream air tank equipped with a pressure sensor to monitor injection pressure stability. Nitrogen was injected through the jet orifice. A two-stage pressure regulator maintained precise air tank pressure control, enabling accurate adjustment of the injection total pressure (Section S1 of the ESM). The injection parameters are summarized in Table 2.

Table 2 Experimental injection parameters

Injection parameters	Symbol	Value
Jet orifice diameter	d	2 mm
Mach number	Ma_j	1
Total temperature	T_{0j}	300 K
Total pressure	P_{0j}	100 kPa 300 kPa 500 kPa
Jet to mainstream dynamic pressure ratio	J	J_1=1.64 J_2=4.92 J_3=8.19

2.2 Experimental observation scheme

Rayleigh and Mie scattering techniques were employed to characterize the typical flow field structures of a transverse jet in supersonic crossflow, a configuration extensively documented in prior studies (Zhao et al., 2009; Yi et al., 2010; Zhao et al., 2010; Zhu et al., 2015). Crucially, both methods could be implemented using identical optical instrumentation by strategically selecting seeding particles of appropriate dimensions.

The integrated Rayleigh/Mie scattering system in this study comprised (a) a dual-cavity pulsed Nd:YAG laser (wavelength 532 nm); (b) a programmable particle generator capable of producing both nanoparticles (TiO_2, 50 nm) for Rayleigh scattering and microparticles (TiO_2, 0.5 μm) for Mie scattering; (c) two charge-coupled device (CCD) cameras (FlowSense EO 11M, 4000 × 2672 pixels, 12-bit dynamic range) equipped with NIKON 60 mm f/2.8 lens and Schimpflug mounts; and (d) a synchronizer controlling laser firing and camera exposure with temporal resolution < 100 ns.

To quantitatively assess PIV image quality and the uniformity of tracer particle seeding, the particle density and spatial distribution within the acquired instantaneous images were evaluated (Section S2 of the ESM). According to the criteria established by Keane and Adrian (Keane and Adrian, 1992), an interrogation window in a double-exposure PIV system should contain no fewer than 10 particles to ensure a sufficiently high detection probability during cross-correlation processing. In the present dataset, 99.7% of the interrogation windows satisfied this criterion, thereby confirming the adequacy of the particle seeding density.

Spatiotemporal resolution was achieved through nanosecond laser pulses (≤6 ns duration) and camera exposures (≤15 μs), enabling transient flow field visualization. The system generated a laser sheet with a minimum thickness of 0.5 mm at the measurement plane. During operation, the synchronizer triggered sequential laser pulses with adjustable interpulse intervals (0.5 – 500 μs) while the camera operated in double-exposure mode. Nanoparticles or microparticles seeded in the upstream region scattered the incident light, with the resulting Rayleigh or Mie scattering signatures captured across two consecutive exposures. Grayscale images of the transverse jet flow field could be acquired from these signatures.

Postprocessing procedures employed DynamicStudio software to extract instantaneous velocity fields or transient flow structures from the grayscale images. The pinhole model was used for camera calibration. A calibration target featuring 24×24 black circular markers was used, with each observation plane serving as the reference plane. The target was displaced at positions of ±2 mm, ±1 mm, and 0 mm relative to this plane. Based on the calibration results, the experimental data were postprocessed. Statistical averaging of multiple velocity field images yielded the scalar velocity field and the three velocity components within the observation area.

To precisely define the position of the observation region, a Cartesian coordinate system was established with its origin at the center of the jet orifice. The x-axis aligned with the mainstream flow direction, while the y-axis followed the wall-normal direction (coinciding with the injection direction). The z-axis was determined by the right-hand rule. Within this framework, the laser sheet positions were specified as the XOY and YOZ slices, as illustrated in Fig. 2.

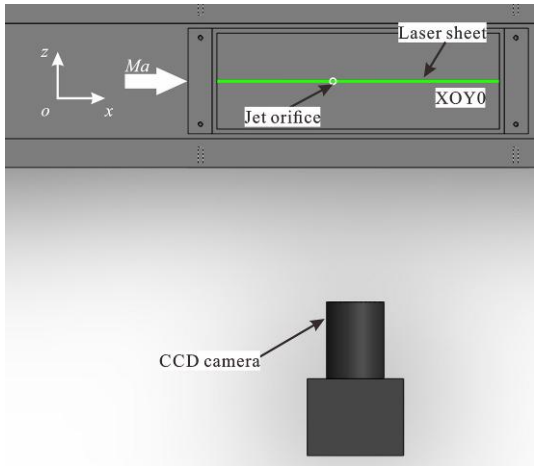

(a) XOY slice location

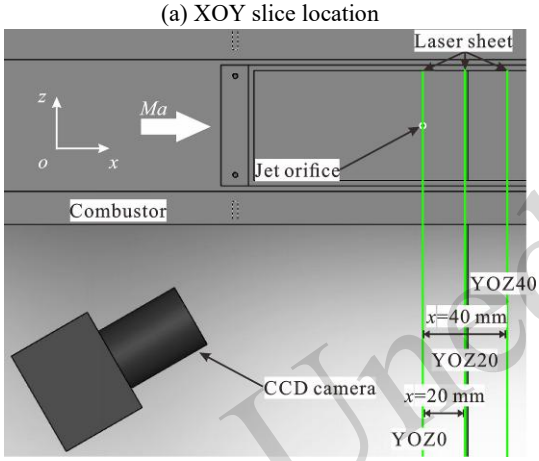

(b) YOZ slice location

Fig. 2 Observation area scheme for Rayleigh/Mie scattering

The experimental observation conditions are summarized in Table 3. Here, XOY0 denoted the XOY slice passing through the orifice center, and YOZ20 referred to the YOZ slice located 20 mm downstream of the orifice.

Table 3 Regional observation and arrangement of optical diagnostic methods

Label	Observation area position	Optical diagnostic techniques
XOY0	z=0 mm	Rayleigh/Mie scattering, stereo-PIV
YOZ0	x=0 mm	Rayleigh/Mie scattering, stereo-PIV
YOZ5	x=5 mm	Rayleigh/Mie scattering
YOZ10	x=10 mm	Rayleigh/Mie scattering, stereo-PIV
YOZ20	x=20 mm	Rayleigh/Mie scattering, stereo-PIV
YOZ40	x=40 mm	Rayleigh/Mie scattering, stereo-PIV
YOZ60	x=60 mm	stereo-PIV
YOZ80	x=80 mm	stereo-PIV
YOZ100	x=100 mm	Rayleigh/Mie scattering

Transient flow structures and PIV velocity fields could be directly acquired from the XOY slice, as undistorted imaging is achievable in this orientation (Fig. 2(a)). In contrast, observations in the YOZ slice provided critical insights into the transverse jet flow field but necessitated oblique imaging with a Scheimpflug adapter to maintain focus across the inclined field of view (Fig. 2(b)). This configuration introduced perspective distortion, requiring geometric correction of raw particle images prior to flow structure analysis. For three-dimensional velocity reconstruction in the YOZ slice, stereo-PIV using two cameras observing the same region was essential. The velocity components in the spatial coordinate system were resolved through a least-squares solution of displacement vectors from both cameras, as depicted in the dual-camera arrangement in Fig. 3.

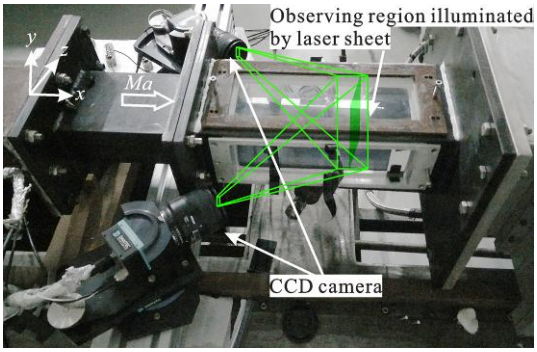

Fig. 3 Diagram of YOZ Slice Observation using Two CCD Cameras for Stereo-PIV

3 Results and discussion

3.1 Assessment of Particle Density

Comparative experiments were conducted to analyze the flow characteristics of particle-laden jets versus unladen jets. Fig. 4 presents grayscale images of the transient flow structures in the XOY0 slice.

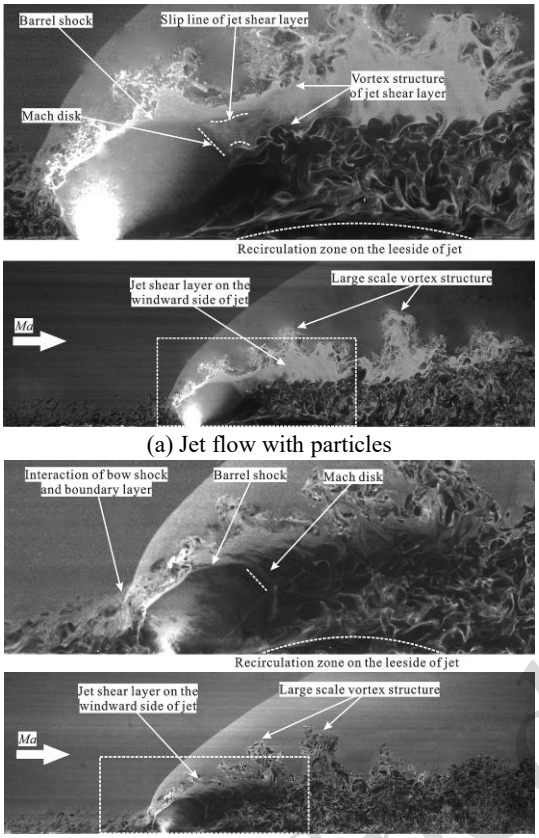

(a) Jet flow with particles

(b) Jet flow without particles

Fig. 4 Gray images of the XOY0 slice in comparative experiments

As shown in Fig. 4(a) and (b), the introduction of tracer particles significantly enhances the grayscale intensity within the shear layer, thereby improving flow visualization. Distinct flow features, including the barrel shock, Mach disk, and slip line, become clearly identifiable after particle seeding. The velocity gradient at the jet shear layer induces a slip line, while Kelvin-Helmholtz (K-H) instability rapidly destabilizes the flow, generating large-scale eddies that fragment within short streamwise distances. Concurrently, strong shear stresses between the high-speed crossflow and jet fluid drive the entrainment of windward-side jet fluid into the leeward side, forming a CVP. This dynamic interaction creates an extended recirculation zone downstream of the jet, which facilitates critical fuel-air mixing for flame stabilization and ignition. In the subsequent experiments of this study, tracer particles were seeded into both the mainstream and the jet flows to enhance the optical diagnostic results of the detailed flow field.

To characterize the three-dimensional topology of the transverse jet and investigate the evolution dynamics of streamwise vortices, a sequence of instantaneous grayscale images was acquired across multiple YOZ slices. Fig. 5(a) captures the transient flow structure in the YOZ0 slice intersecting the jet orifice center. The initially underexpanded jet flow undergoes rapid expansion, forming a barrel-shaped shock wave that exhibits a fan-like geometry in the YOZ cross-section. The inner inflection point of this shock structure aligns with computational fluid dynamics (CFD) predictions by Liang et al.(Liang et al., 2020), confirming its role as a critical flow feature. The fluid undergoes rapid expansion and acceleration within the barrel shock, leading to a swift decrease in density and a concomitant reduction in its gray value. As illustrated in Fig. 5(b), within the YOZ5 slice, the shear layer on the windward side of the jet undergoes continuous development. Fluid starts to be entrained from both sides of the barrel shock into the region beneath the plume. Simultaneously, the lee-side shock interacts with the vortical structures, leading to the formation of a recirculation zone on the leeward side. Within the YOZ10 slice of Fig. 5(c), the shear layer on the windward side of the jet manifests fragmented vortical structures. The spatial extent of the barrel shock region diminishes, while its specific morphological features become indistinguishable.

The barrel shock wave dissipates in the YOZ20 slice, indicating that pressure matching has been achieved between the jet and the surrounding fluid. Strong entrainment by the CVP transports windward-side fluid toward the leeward side, forming the prominent CVP. The vortex cores of the CVP exhibit reduced grayscale intensity due to localized density and pressure minima, which can be clearly discerned in Fig. 5(d). The plume becomes dominated by the CVP, and vortex shedding is observed in the windward-side shear layer.

Fig. 5(e) displays the flow structure in the YOZ40 slice, where the jet plume has completely broken down. By YOZ100 (Fig. 5(f)), the jet plume exhibits significant vertical uplift and an expanded plume scope, a signature of persistent fluid entrainment despite the complete disintegration of streamwise vortices. The unresolved CVP vortices indicate a transition to small-scale turbulent mixing,

evidenced by diminishing coherence in the vorticity structure. This morphological evolution confirms that vorticity-driven entrainment continues to enhance the jet penetration depth and lateral diffusion even after large-scale vortex breakdown.

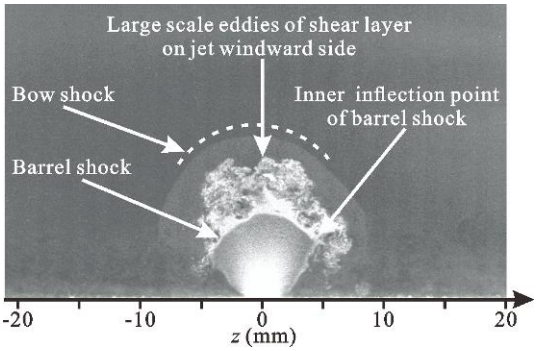

(a) YOZ0

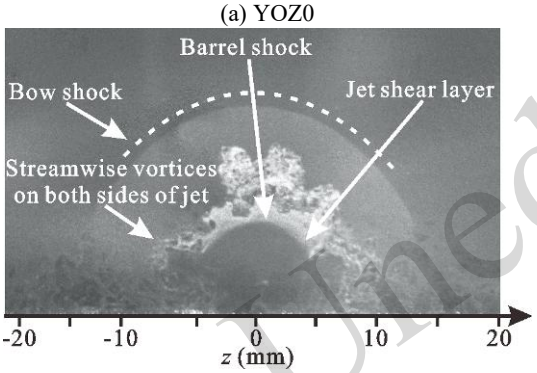

(b) YOZ5

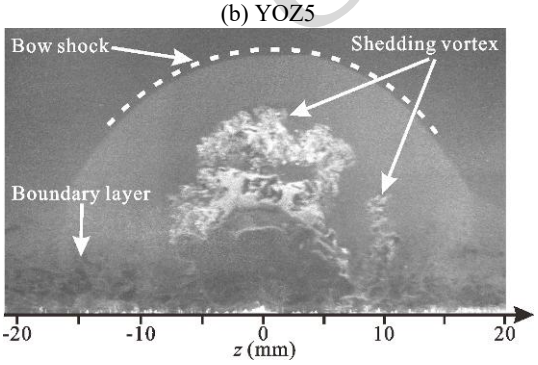

(c) YOZ10

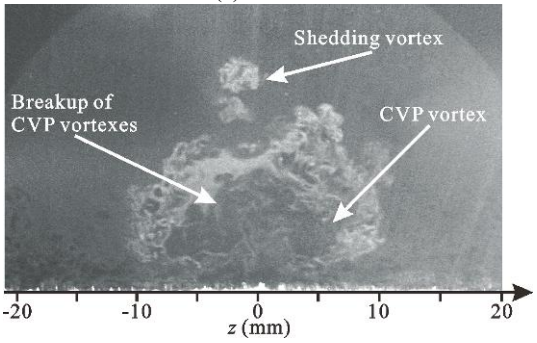

(d) YOZ20

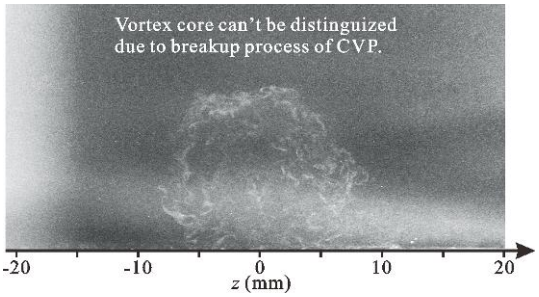

(e) YOZ40

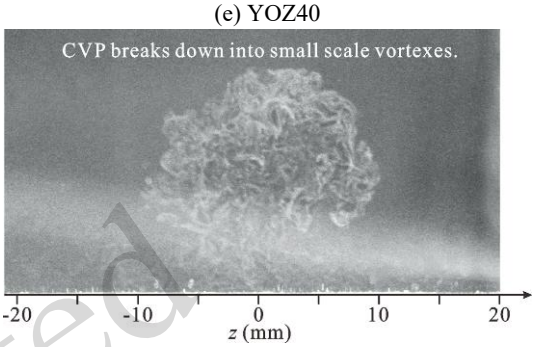

(f) YOZ100

Fig. 5 Instantaneous grayscale images of YOZ slices in the transverse jet flow field

3.2 Velocity distribution analysis

Transient velocity distributions were obtained by postprocessing particle image pairs from the experimental data. The mean velocity was subsequently determined by averaging 100 transient distributions, as illustrated in Fig. 6. Vorticity fields were then calculated from the mean velocity distribution using Eq. (1).

$$\omega = \nabla \times \boldsymbol{V} = \frac{\partial \boldsymbol{V}_y}{\partial x} - \frac{\partial \boldsymbol{V}_x}{\partial y}, \tag{1}$$

where ω denotes the local vorticity, $\boldsymbol{V}_y$ represents the velocity component along the y-axis, and $\boldsymbol{V}_x$ signifies the velocity component along the x-axis.

The average velocity distribution of the XOY0 slice is presented in Fig. 6(a), revealing a barrel shock length of approximately 8 mm and a recirculation zone length of approximately 20 mm on the leeward side of the jet. Considering the transient flow field structure previously noted, a CVP formed at the YOZ20 slice, which subsequently dominated the transverse jet flow field. The y-axis velocity component is displayed in Fig. 6(b), illustrating that the bow shock induces deflection of the incoming flow. However, a fraction of the fluid is redirected by the expansion wave located downstream of the bow shock, thereby inducing a velocity component

oriented along the -y direction. Near the jet exit, the jet plume manifests a pronounced $+y$ velocity component, which provides the initial momentum required for downstream jet penetration. Furthermore, the induction effect exerted by the CVP contributes to a progressive uplift of the plume.

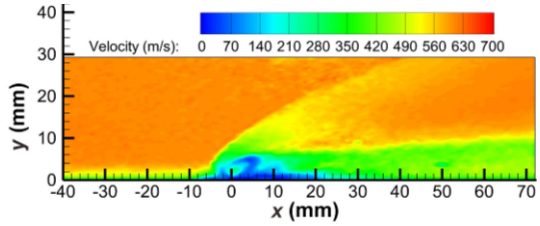

(a) Distribution of mean scalar velocity

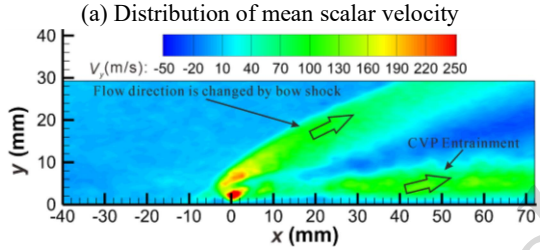

(b) Average y-axis velocity component

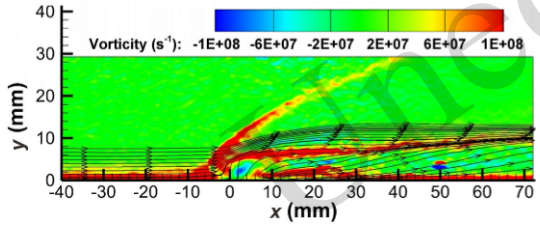

(c) Mean vorticity field

Fig. 6 Fields of average velocity and vorticity for the XOY0 slice

Fig. 6(c) presents the computed mean vorticity field and corresponding streamline distribution derived from the instantaneous velocity data. Significant spanwise vorticity is generated primarily within high-shear regions on both the windward and leeward sides of the jet. The windward shear layer originates from the local velocity gradient between the incoming crossflow and the jet, while the leeward shear is dominated by frictional effects due to viscous interactions between the wall and the fluid entrained beneath the CVP. Streamline analysis reveals that the upstream crossflow converges with the jet fluid along the windward side, identifying this region as a critical zone for shear layer formation and enhanced mixing processes.

The evolution of the transverse jet is primarily governed by streamwise vortices, rendering the vorticity field on the YOZ cross-section particularly informative for analyzing the development of these vortices. Analysis of the vorticity fields and velocity contours across different YOZ slices (Fig. 7) reveals that the development of the CVP exerts a pivotal influence on the evolution of streamwise vortices. The CVP of the jet plume commences its formation at the jet orifice, as evidenced by the vorticity field in Fig. 7(a); however, the induced vortices beneath the CVP remain comparatively feeble at this initial stage. Within the near-field mixing region, the CVP vortices transition into a roll-up phase. During this process, ambient fluid is entrained into the plume and undergoes rapid mixing with the jet fluid under intense shear stress, resulting in a gradual enlargement of the CVP. Concurrently, a pair of vortices exhibiting opposite vorticity is induced beneath the CVP, as illustrated in Fig. 7(b) and (c).

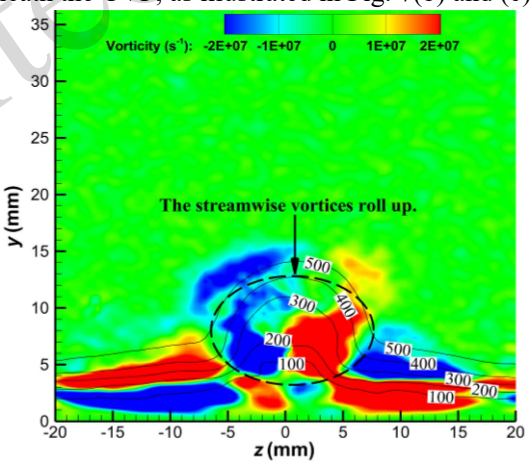

(a) YOZ0

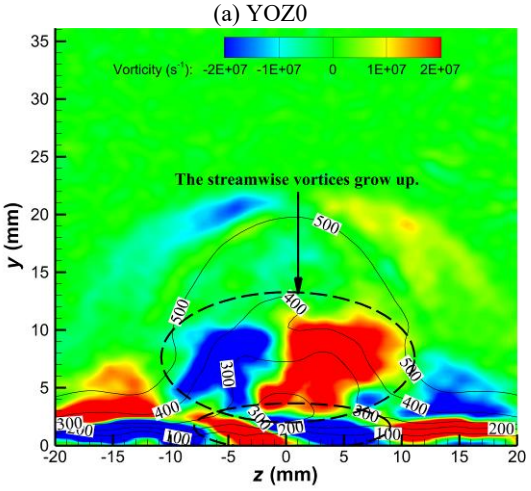

(b) YOZ10

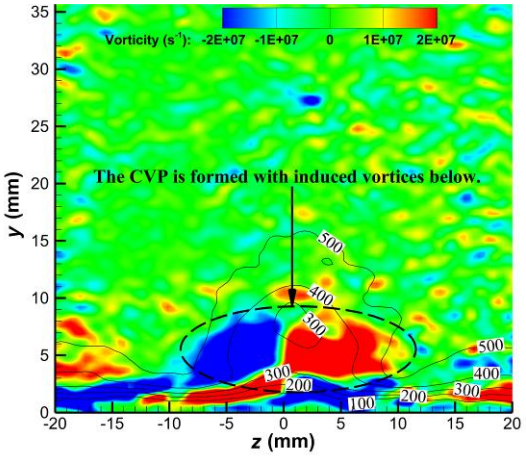

(c) YOZ20

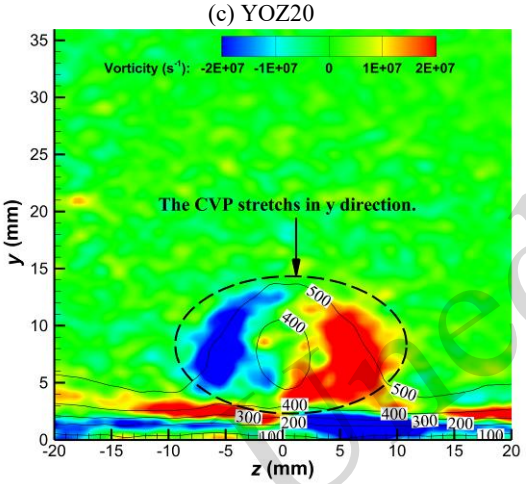

(d) YOZ40

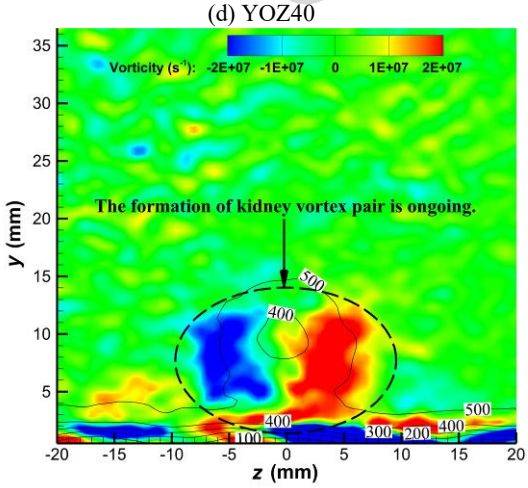

(e) YOZ60

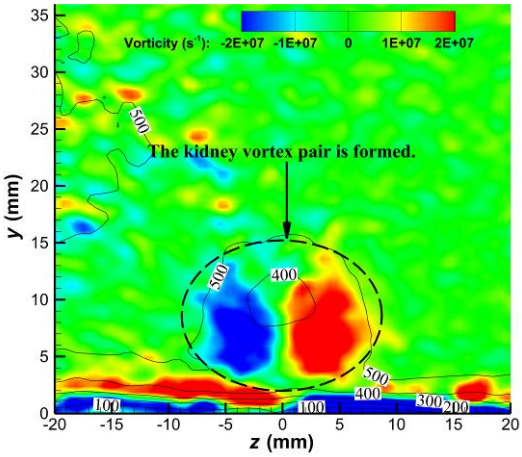

(f) YOZ80

Fig. 7 Maps of vorticity distribution and velocity contours across various YOZ slices

As the flow progresses into the far-field mixing region, the CVP vortices undergo progressive stretching in the y-direction, leading to an expansion of their influence domain (Fig. 7(d)). As the jet plume develops downstream, fluid mixing between the jet and crossflow becomes dominated by CVP-induced entrainment mechanisms. Progressive morphological changes in the vortical structure are evident: The CVP expands spatially while undergoing axial distortion, as observed in Fig. 7(e) and (f). Each vortex within the pair elongates vertically while maintaining separation, ultimately forming a characteristic kidney-shaped vortex pair configuration.

3.3 Penetration and lateral diffusion

The boundaries of jet penetration and lateral diffusion are critical for characterizing the mixing performance of transverse jets in supersonic crossflow. Portz et al. (Portz and Segal, 2006) systematically analyzed key factors influencing transverse jets in high-speed flows and derived the empirical penetration depth correlation expressed in Eq. (2).

$$P/d = AJ^{B}\left(x/d + C\right)^{E}\left(\delta/d\right)^{F}\left(Ma_j/Ma_\infty\right)^{G}, \quad (2)$$

where d is the jet orifice diameter, P/d is the dimensionless penetration depth, J is the dynamic pressure ratio, x/d is the dimensionless distance from the jet orifice, δ/d is the dimensionless boundary layer thickness, Ma is the Mach number, the subscript j represents the jet parameter, the subscript ∞ stands

for the mainstream flow parameter, and *A, B, C, E, F,* and *G* are the fitting coefficients.

Eq. (2) was simplified by Sun et al. (Sun et al., 2013a) by neglecting the influence of the boundary layer thickness, yielding Eq. (3).

$$P/d = AJ^B\left(x/d + C\right)^E \tag{3}$$

To investigate the influence of boundary layer thickness on flow dynamics, two experimental configurations with distinct nozzle-to-orifice distances were implemented. The boundary layer thickness was demonstrated to be δ = 1 mm and δ = 4 mm (Section S3 of the ESM).

The Rayleigh/Mie scattering system was employed to capture transient grayscale images of the transverse jet flow field under varying boundary layer thickness conditions, in accordance with the methodology established by Gruber et al. (Gruber, et al., 1997). The high spatial resolution of the measurement system ensured that the boundaries of the jet plume could be clearly identified in the transient images (Section S4 of the ESM).

The jet penetration depths are plotted against the dynamic pressure ratio and boundary layer thickness. A bivariate linear regression analysis was subsequently applied to determine the statistically significant fitting coefficients for Eq. (2), establishing an empirical correlation between penetration depth and these control variables. The fitting coefficients of the present study and two previous studies are presented in Table 4.

Table 4 Fitting coefficients of the penetration formula in different studies

Fitting coefficients	Present study	Sun (Sun et al., 2013b)	Ron Portz (Portz and Segal, 2006)
A	2.084	2.933	1.362
B	0.442	0.256	0.568
C	0	0	-1.5
E	0.149	0.161	0.276
F	0.092	0	0.221
G	0	0	-0.0251

Fig. 8 superimposes the fitted penetration depth curves from this study onto experimental scatter plots, demonstrating quantitative alignment across all dynamic pressure ratios and boundary layer thicknesses. An increase in boundary layer thickness enhances the jet penetration depth in the far field by approximately 10–20% across varying dynamic pressure ratios.

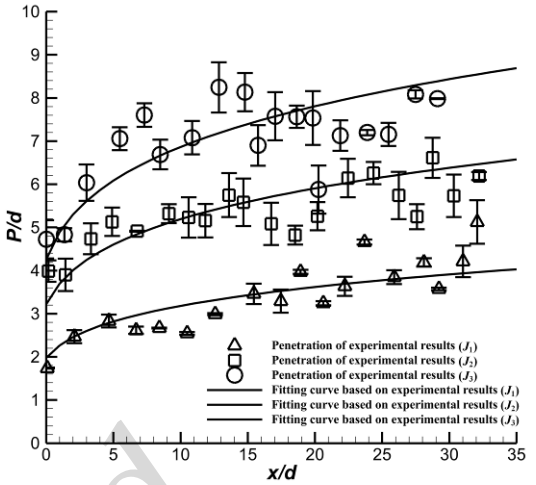

(a) Boundary layer thickness: 1 mm

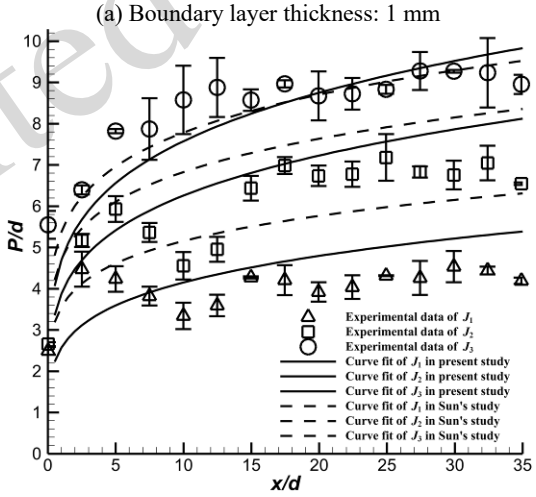

(b) Boundary layer thickness: 4 mm

Fig. 8 Penetration depth variation of a transverse jet in supersonic crossflow for different boundary layer thicknesses

For comparison, the correlation proposed by Sun et al. (Sun, et al., 2013a) is plotted in Fig. 8(b). While their model exhibits strong agreement with experimental data at high dynamic pressure ratios, it systematically overestimates penetration depths at lower ratios. This deviation underscores the critical influence of boundary layer thickness, a parameter not explicitly accounted for in the formulation of Sun et al.'s, on jet penetration dynamics.

Fig. 9 compares the penetration depth correlations derived in this study with those of Portz et al.(Portz and Segal, 2006) across varying boundary layer thicknesses and dynamic pressure ratios. Both models demonstrate consistent predictions when the

boundary layer thickness and dynamic pressure ratio are relatively low. However, as these parameters increase, the correlation from Portz et al. yields progressively larger deviations, overestimating penetration depths compared with experimental measurements.

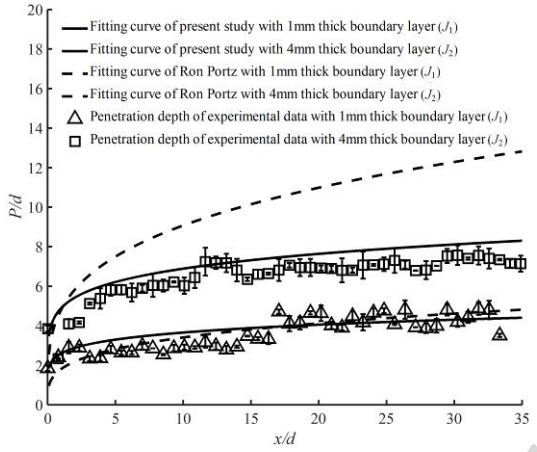

Fig. 9 Comparative analysis of penetration depth predictions: Current study vs. Ron Portz's research (Portz and Segal, 2006)

The lateral spreading of the jet plume was quantified by its maximum width along both lateral boundaries, which was unambiguously identified from transient grayscale images of YOZ slices. For each YOZ slice, the plume width was extracted from 100 transient grayscale images to form a statistical ensemble. The lateral diffusion boundaries were determined using the same edge-detection methodology applied to penetration depth quantification. Fig. 10 illustrates the lateral diffusion boundaries across all YOZ slices (annotated by streamwise position x).

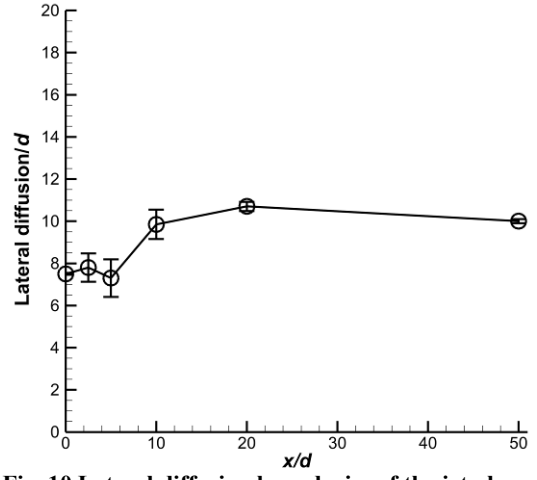

Fig. 10 Lateral diffusion boundaries of the jet plume ($\delta_{0.99}$=4 mm, J=4.92)

Due to strong jet underexpansion, lateral spreading peaks at approximately 7.5d (15 mm) near the jet orifice centerline (x=0). This dimension remains nearly constant over a short development length of 5d (10 mm), followed by rapid expansion to 10d (20 mm) at x=10d. Beyond this location, lateral diffusion exhibits negligible augmentation (<3% increase per d). This behavior indicates the following:

(a) Initial plume expansion dominates lateral spreading within x<10d, driven primarily by pressure-gradient effects.

(b) Streamwise vortex development enhances lateral mixing up to x=10d through entrainment amplification.

(c) Kinetic energy dissipation and vorticity decay beyond x=10d eliminate driving mechanisms for further spreading, resulting in asymptotic stabilization of lateral dimensions.

3.4 Assessment of jet plume breakup

Owing to the absence of tracer particles within the jet flow, its grayscale value approximates zero. In contrast, the mainstream flow demonstrates uniformly high grayscale intensity due to homogeneous particle seeding. Given the superior tracing fidelity of nanoparticles, grayscale variations in the images precisely reflect the intermixing process between the jet flow and mainstream flow. Edge detection algorithms are capable of identifying the interfacial boundary where the jet fluid and mainstream fluid interact. Fractal dimension analysis then offers a quantitative metric for plume fragmentation intensity—higher degrees of fragmentation signify expanded interfacial areas and enhanced completeness of mixing.

Transient grayscale images underwent edge detection using the Canny operator. The fractal dimension of the transverse jet flow under varying boundary layer thicknesses was subsequently calculated via the box-counting method (Zhu, et al., 2015; Zhao et al., 2016). For statistical robustness, each of the 100 grayscale frames was segmented into 45 sections, and the fractal dimension of each section was computed. Fig. 11 illustrates the streamwise distribution of the fractal dimension averaged across all 100 frames, providing a quantitative assessment

of the jet plume fragmentation process.

The spatial distribution of the fractal dimension can be categorized into three distinct regions, as illustrated in Fig. 11. In this figure, the Dim on the y-axis refers to the fractal dimension. Region I is situated immediately upstream of the jet orifice. Region II corresponds to the near-field mixing zone, while Region III represents the far-field mixing region (Ben-Yakar et al., 2006b).

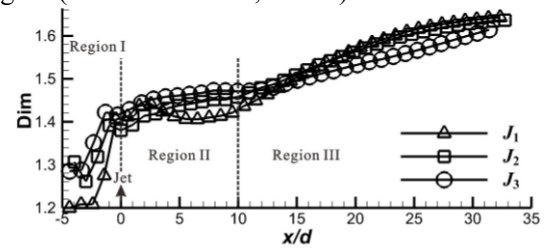

(a) Boundary layer thickness: 1 mm

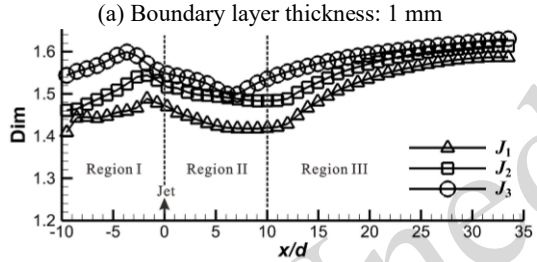

(b) Boundary layer thickness: 4 mm

Fig. 11 Streamwise distribution of the fractal dimension in the XOY0 slice for two boundary layer thicknesses

Due to the thin boundary layer of only 1 mm, the initial fractal dimension in Region I is notably low. The fractal dimension exhibits contrasting trends across these regions: a sharp increase in Region I, as depicted in Fig. 11(a). The abrupt surge is attributed to complex vortex structures generated by shock-boundary layer interactions. In Region II, the fractal dimension displays a gradual increase under high dynamic pressure ratios but experiences a slight decline at low dynamic pressure ratios. This behavior likely stems from the competition between reduced vortex merging and enhanced eddy generation on the windward side of the jet. Within Region III, the CVP develops and subsequently breaks down, driving the rapid increase in fractal dimension.

Fig. 11(b) illustrates the streamwise distribution of the fractal dimension in the transverse jet flow field under a boundary layer thickness of 4 mm. In Region I, the interaction between the bow shock and the boundary layer induces a large separation zone and complex vortical structures, leading to a noticeable increase in the fractal dimension. Nevertheless, the majority of these separated vortical structures fail to penetrate the windward side of the jet; rather, they evolve downstream along both sides of the jet. Consequently, the fractal dimension at the XOY0 slice exhibits an initial increase followed by a subsequent decrease. In Region II, large-scale vortical structures emerge and roll up along the jet's windward shear layer, driven by the pronounced velocity gradient imposed by the interaction of the transverse jet and mainstream flow. These structures enlarge progressively; nevertheless, fluid on the windward side is continuously entrained toward the leeward side by the CVP. Owing to the relatively weaker shear effect on the leeward side, the breakdown of vortical structures proceeds at a slower rate, resulting in an initial decline in the fractal dimension followed by a gradual recovery. In Region III, the progressive disintegration of the jet shear layer drives further fragmentation of vortical structures on both the windward and leeward sides under the CVP-dominated entrainment process. The fractal dimension of the jet plume exhibits a continuous increase until attaining its maximum magnitude.

Comparative analysis of Fig. 11(a) and (b) indicates that boundary layer thickness exerts a primary role in influencing Region I and Region II, governed by three interrelated mechanisms: (i) Shock-boundary layer interactions induce complex vortex structures, thereby augmenting the fractal dimension; (ii) The evolution of the streamwise vortex system generates large-scale vortex configurations via induction and fragmentation, elevating the fractal dimension, whereas vortex merging leads to its reduction; (iii) Jet mixing processes trigger vortex dissipation, resulting in a gradual reduction of the fractal dimension. Consequently, the fractal dimension is predominantly governed by the competition among these specific mechanisms within the complex flow field. Fig. 11 indicates that a thicker boundary layer intensifies jet-mainstream interactions in Region I, resulting in higher fractal dimensions. Although the jet flow is dominated by the CVP in Region III, the fractal dimension values of the jet plume remain remarkably consistent across varying boundary layer

thicknesses.

4. Conclusions

In this study, Rayleigh/Mie scattering and stereoscopic particle image velocimetry were employed to characterize the transient flow field structure and vorticity dynamics of a jet in supersonic crossflow. The key findings are summarized as follows.

Transient Flow field Topology: The morphological characteristics were successfully visualized, including the jet barrel shock waves, Mach disks, shear layers, slip lines, and leeward surface recirculation zones. The vortex structure on the windward side of the jet is highly nonuniform under intensive shear forces. Driven by the Kelvin-Helmholtz instability, this structure progressively destabilizes, leading to the formation of rapidly mixed shear layers that collapse within a short flow distance.

Vortex System Evolution: The vorticity field reveals a multivortex system emerging in the near-field mixing region. The formation of a counterrotating vortex pair initiates approximately 20 mm downstream of the orifice, induced by shear stress along the barrel shock periphery. Downstream development features vertical elongation of individual streamwise vortices while maintaining spatial separation, culminating in a characteristic kidney-shaped vortex pair.

Jet Penetration and Spreading: The boundary layer thickness significantly enhances the penetration depth, with the empirical correlations correcting prior model overpredictions under thick boundary layer conditions (4 mm). Strong jet underexpansion drives peak lateral spreading (15 mm) at the orifice centerline. Rapid expansion to 20 mm occurs 20 mm downstream from the jet orifice, followed by saturation (<3% increase per 2 mm) due to diminished vorticity-driven entrainment.

Plume Fragmentation Quantification: The streamwise distribution of the fractal dimension delineates three distinct regions. Region I: A sharp increase driven by shock boundary layer interaction-generated vortex complexity. Region II: The trend is governed by competition between vortex merging (suppressing fractality) and windward-side eddy generation (enhancing fractality). Region III: A rapid ascent to peak values (approximately 1.6) due to counterrotating vortex pair fragmentation under the dominance of mainstream-jet shear stress.

Acknowledgments

The authors gratefully acknowledge the support provided by the Program of National Key Laboratory of Ramjet (Grant No. STS/MY-ZY-2020-007 and No. 2023-JCJQ-LB-018-05).

Author contributions

Yanhui ZHAO completed the main research work and wrote the initial draft; Zhenfeng WANG guided the experimental scheme; Shunping ZHANG assisted in the experimental work and data processing; Shimao WANG helped to organize the manuscript; Xuechen LI provided the measurement equipment and assisted in the layout and debugging of the experimental observation system; Ye TIAN revised and edited the final version.

Conflict of interest

Yanhui ZHAO, Zhenfeng WANG, Shunping ZHANG, Shimao WANG, Xuechen LI and Ye TIAN declare that they have no conflicts of interest.

References

Anokhin MD, Vinogradov YA, Zubkov AI, et al., 1998. Determination of the shape of the shocks ahead of a transverse jet injected into a supersonic flow. Fluid dynamics, 33(2):186-189. https://doi.org/10.1007/BF02698700

Ben-Yakar A, Mungal MG, Hanson RK, 2006a. Time evolution and mixing characteristics of hydrogen and ethylene transverse jets in supersonic crossflows. Physics of Fluids, 18(2) https://doi.org/10.1063/1.2139684

Ben-Yakar A, Mungal MG, Hanson RK, 2006b. Time evolution and mixing characteristics of hydrogen and ethylene transverse jets in supersonic crossflows. Physics of Fluids, 18, 026101 https://doi.org/10.1063/1.2139684

Erdem E, Kontis K, 2021. Experimental investigation of sonic transverse jets in mach 5 crossflow. Aerospace Science and Technology, 110:18. https://doi.org/10.1016/j.ast.2020.106419

Fries D, Ranjan D, Menon S, 2021. Turbulent mixing and trajectories of jets in a supersonic cross-flow with different injectants. Journal of Fluid Mechanics, 911:40. https://doi.org/10.1017/jfm.2020.1065

Gamba M, Mungal MG, 2015. Ignition, flame structure and near-wall burning in transverse hydrogen jets in supersonic crossflow. Journal of Fluid Mechanics, 780:226-273. https://doi.org/10.1017/jfm.2015.454

Glagolev AI, Zubkov AI, Panov YA, 1967. Supersonic flow past a gas jet obstacle emerging from a plate. Fluid dynamics, 2(3):60-64. https://doi.org/10.1007/BF01027359

Glagolev AI, Zubkov AI, Panov YA, 1971. Interaction between a supersonic flow and gas issuing from a hole in a plate. Fluid dynamics, 3(2):65-67. https://doi.org/10.1007/BF01013556

Gruber MR, Nejad AS, Chen TH, et al., 1997. Compressibility effects in supersonic transverse injection flow fields. Physics of Fluids, 9(5):1448-1448. https://doi.org/10.1063/1.869257

Huang W, Yan L, 2013. Progress in research on mixing techniques for transverse injection flow fields in supersonic crossflows. Journal of Zhejiang University-Science A, 14(8):554-564. https://doi.org/10.1631/jzus.A1300096

Huang W, 2016. Transverse jet in supersonic crossflows. Aerospace Science and Technology, 50:183-195. https://doi.org/10.1016/j.ast.2016.01.001

Huang W, Du Z-B, Yan L, et al., 2019. Supersonic mixing in airbreathing propulsion systems for hypersonic flights. Progress in Aerospace Sciences, 109 https://doi.org/10.1016/j.paerosci.2019.05.005

Huang W, Chang JT, Yan L, 2020. Mixing and combustion in supersonic/hypersonic flows. Journal of Zhejiang University-Science A, 21(8):609-613. https://doi.org/10.1631/jzus.A20MCSF1

Iwasa T, Tsuboi N, 2022. Numerical simulation of jet mixing in supersonic crossflow: Effect of jet exit geometry. Transactions of the Japan Society for Aeronautical and Space Sciences, 65(4):172-184. https://doi.org/10.2322/tjsass.65.172

Jia DP, Yang K, Pan Y, et al., 2022. Effect of the micro vortex generator on the characteristics of vaporized rp-3 kerosene combustion in supersonic flows. Journal of Zhejiang University-Science A, 23(5):405-414. https://doi.org/10.1631/jzus.A2000620

Keane RD, Adrian RJ, 1992. Theory of cross-correlation analysis of piv images. Applied Scientific Research, 49(3):191-215. https://doi.org/10.1007/BF00384623

Liang C-H, Sun M-B, Liu Y, et al., 2020. Numerical study of flow structures and mixing characteristics of a sonic jet in supersonic crossflow. Acta Astronautica, 166:78-88. https://doi.org/10.1016/j.actaastro.2019.10.008

Liao L, Yan L, Huang W, et al., 2018. Mode transition process in a typical strut-based scramjet combustor based on a parametric study. Journal of Zhejiang University-Science A, 19(6):431-451. https://doi.org/10.1631/jzus.A1700617

Liu C, Wang Z, Wang H, et al., 2015. Numerical investigation on mixing and combustion of transverse hydrogen jet in a high-enthalpy supersonic crossflow. Acta Astronautica, 116:93-105. https://doi.org/10.1016/j.actaastro.2015.06.023

Liu C, Yu J, Wang Z, et al., 2019. Characteristics of hydrogen jet combustion in a high-enthalpy supersonic crossflow. Physics of Fluids, 31(4) https://doi.org/10.1063/1.5084751

Liu Y, Sun M-B, Liang C-H, et al., 2018. Structures of near-wall wakes subjected to a sonic jet in a supersonic crossflow. Acta Astronautica, 151:886-892. https://doi.org/10.1016/j.actaastro.2018.07.048

Liu Y, Sun MB, Yang YX, et al., 2020. Turbulent boundary layer subjected to a sonic transverse jet in a supersonic flow. Aerospace Science and Technology, 104:10. https://doi.org/10.1016/j.ast.2020.106016

Mahesh K, 2013. The interaction of jets with crossflow. Annual Review of Fluid Mechanics, 45:379-407. https://doi.org/10.1146/annurev-fluid-120710-101115

Portz R, Segal C, 2006. Penetration of gaseous jets in supersonic flows. Aiaa Journal, 44(10):2426-2429. https://doi.org/10.2514/1.23541

Santiago JG, Dutton JC, 1997. Velocity measurements of a jet injected into a supersonic crossflow. Journal of Propulsion and Power, 13(2):264-273.

Shi W, Tian Y, Zhang WZ, et al., 2020. Experimental investigation on flame stabilization of a kerosene-fueled scramjet combustor with pilot hydrogen. Journal of Zhejiang University-Science A, 21(8):663-672. https://doi.org/10.1631/jzus.A1900565

Steinberg AM, Sadanandan R, Dem C, et al., 2013. Structure and stabilization of hydrogen jet flames in cross-flows. Proceedings of the Combustion Institute, 34:1499-1507. https://doi.org/10.1016/j.proci.2012.06.026

Sun M-B, Hu Z-W, 2018a. Mixing in nearwall regions downstream of a sonic jet in a supersonic crossflow at mach 2.7. Physics of Fluids, 30(10) https://doi.org/10.1063/1.5045752

Sun M, Zhang S, Zhao Y, et al., 2013a. Experimental investigation on transverse jet penetration into a supersonic turbulent crossflow. Science China-Technological Sciences, 56(8):1989-1998. https://doi.org/10.1007/s11431-013-5265-7

Sun M, Zhang S, Zhao Y, et al., 2013b. Experimental investigation on transverse jet penetration into a supersonic turbulent crossflow. Science China Technological Sciences, 56(8):1989-1998. https://doi.org/10.1007/s11431-013-5265-7

Sun MB, Hu ZW, 2018b. Generation of upper trailing counter-rotating vortices of a sonic jet in a supersonic crossflow. Aiaa Journal, 56(3):1047-1059. https://doi.org/10.2514/1.J056442

Sun YC, Cai Z, Wang TY, et al., 2020. Numerical study on cavity ignition process in a supersonic combustor. Journal of Zhejiang University-Science A, 21(10):848-858. https://doi.org/10.1631/jzus.A1900419

Vinogradov YA, Zhilenko DY, Zubkov AI, et al., 1999. Flow pattern in the vicinity of an annular system of transverse jets in a supersonic stream. Fluid dynamics, 34(1):17-22. https://doi.org/10.1007/BF02698745

Viti V, Neel R, Schetz JA, 2009. Detailed flow physics of the supersonic jet interaction flow field. Physics of Fluids, 21(4) https://doi.org/10.1063/1.3112736

Wang H, Wang Z, Sun M, et al., 2013. Hybrid reynolds-averaged navier-stokes/large-eddy simulation of

jet mixing in a supersonic crossflow. Science China-Technological Sciences, 56(6):1435-1448. https://doi.org/10.1007/s11431-013-5189-2

Yi S, Tian L, Zhao Y, et al., 2010. Aero-optical aberration measuring method based on npls and its application. Chinese Science Bulletin, 55(31):3545-3549. https://doi.org/10.1007/s11434-010-4104-5

Zhang H, Xiao Y, He K, et al., 2025. The 3d flow characteristics of a sonic transverse jet in laminar supersonic crossflow. Aerospace Science and Technology, 167 https://doi.org/10.1016/j.ast.2025.110661

Zhang JC, Sun MB, Wang ZG, et al., 2021a. Stabilization mechanisms of lifted flames in a supersonic stepped-wall jet combustor. Journal of Zhejiang University-Science A, 22(4):314-330. https://doi.org/10.1631/jzus.A2000087

Zhang L, Cao Y, Liang J, et al., 2023. Effects of inflow velocity on transverse jet injection in a supersonic cavity combustor. Physics of Fluids, 35(11) https://doi.org/10.1063/5.0177228

Zhang Z, Mccreton SF, Awasthi M, et al., 2021b. The flow features of transverse jets in supersonic crossflow. Aerospace Science and Technology, 118:14. https://doi.org/10.1016/j.ast.2021.107058

Zhao Y-H, Liang J-H, Zhang S-P, et al., 2020. Experimental investigation on flow characteristics of a transverse jet with an upstream vortex generator. Journal of Zhejiang University-Science A, 21(8):636-651. https://doi.org/10.1631/jzus.A1900392

Zhao Y, Yi S, Tian L, et al., 2009. Supersonic flow imaging via nanoparticles. Science in China, Series E: Technological Sciences, 52(12):3640-3648. https://doi.org/10.1007/s11431-009-0281-3

Zhao Y, Yi S, Tian L, et al., 2010. Density field measurement and approximate reconstruction of supersonic mixing layer. Chinese Science Bulletin, 55(19):2004-2009. https://doi.org/10.1007/s11434-010-3222-4

Zhao Y, Liang J, Zhao Y, 2016. Vortex structure and breakup mechanism of gaseous jet in supersonic crossflow with laminar boundary layer. Acta Astronautica, 128:140-146. https://doi.org/10.1016/j.actaastro.2016.06.019

Zhu Y, Yi S, Gang D, et al., 2015. Visualisation on supersonic flow over backward-facing step with or without roughness. Journal of Turbulence, 16(7):633-649. https://doi.org/10.1080/14685248.2015.1021473

Zubkov AI, Lyagushin BE, Panov YA, et al., 1994. Interaction of a transverse gas jet with supersonic flow in a dihedral. Fluid dynamics, 29(6):872-875. https://doi.org/10.1007/BF02040798

Electronic supplementary materials

Sections S1–S4

中文概要

题　目： 不同边界层条件下超声速来流中横向射流的流场结构与混合特性研究

作　者： 赵延辉[1]，王振锋[2]，张顺平[1]，王世茂[2]，李学臣[2]，田野[2]

机　构： [1]冲压发动机技术全国重点实验室，中国绵阳，621000；[2]跨域飞行交叉技术实验室，中国绵阳，621000

目　的： 本研究旨在通过精细实验观测，量化超燃冲压发动机中超声速横向射流的瞬态流场结构与混合特性。聚焦于揭示射流穿透深度、横向扩散、涡系演化及射流破碎过程，为优化发动机燃烧室设计、增强燃料/空气混合及提升燃烧效率提供关键物理依据和定量数据。

创新点： 1. 采用瑞利/米氏散射技术，获取了包含桶形激波、马赫盘在内的瞬态高分辨率流场结构；2. 结合立体粒子图像测速技术，层析展示了流向涡（CVP）从生成到破碎的三维演化过程；3. 运用边缘检测算法和分形维数分析，定量评估了边界层厚度和动量比对射流穿透、横向扩散及羽流破碎程度的影响。

方　法： 1. 采用直连式超声速风洞开展实验，通过集成化喷管/试验段设计消除装配激波干扰，并利用反射舱调节激光光路以抑制壁面反射（图 2）；2. 综合运用瑞利/米散射与立体粒子图像测速技术，获取横向射流流场的瞬态灰度图像及三维速度场分布（图 5 和图 6）；3. 采用分形维数结合盒式计数法，量化射羽流的破碎程度（图 20）。

结　论： 1.清晰捕捉呈现了桶形激波、马赫盘、剪切层及回流区等超声速横流中横向射流的典型流场特征，揭示了强剪切作用下射流迎风侧涡结构的非定常演化过程。2. 发现反向旋转涡对在射流出口附近开始形成，并在下游逐渐拉伸、抬升，最终演化为典型的"肾形"结构，主导了射流与主流的掺混过程。3. 边界层增厚可显著提升射流在下游的穿透深度，但射流羽流的横向扩散则呈现先快速扩展后趋于不变的变化趋势。4. 基于分形维数将射流破碎分为三个区域：区域 I 受激波/边界层干扰影响破碎程度迅速提升，区域 II 受涡合并与生成竞争机制调控，区域 III 在反向旋转涡对主导下破碎程度持续增强直至峰值。

关键词： 超音速来流中的横向射流；流向涡；穿透深度与横向扩散；分形维数；破碎过程